Electronic structure and magnetic properties of (Fe,Co)-codoped ZnO: Theory and experiment

Debjani Karmakar, T. V. Chandrasekhar Rao, and J. V. Yakhmi
Technical Physics Division, Bhabha Atomic Research Center, Mumbai 400085, India

A. Yaresko and V. N. Antonov
Max-Planck-Institut für Festkörperforschung, Heisenbergstraße 1, D-70569 Stuttgart, Germany

R. M. Kadam
Radiochemistry Division, Bhabha Atomic Research Center, Mumbai 400085, India

S. K. Mandal, R. Adhikari, A. K. Das, and T. K. Nath
Department of Physics and Meteorology, Indian Institute of Technology, Kharagpur 721302, India

Nirmal Ganguli and I. Dasgupta
Department of Solid State Physics, Indian Association for the Cultivation of Science, Kolkata 700032, India

G. P. Das
Department of Material Science, Indian Association for the Cultivation of Science, Kolkata 700032, India
(Received 25 February 2010; revised manuscript received 30 April 2010; published 19 May 2010)

We investigate the magnetic behavior of (Fe,Co) codoped ZnO both theoretically and experimentally. The electronic structure calculation for both bulk and cluster systems of codoped ZnO, within the framework of DFT+U, stabilizes in a ferrimagnetic configuration for nearest-neighbor position of the codopants. The exchange properties of the codoped system are dependent on the distance and concentration of the dopants. The theoretical calculations also reveal the importance of defect states in mediating the long-range magnetic order in such systems. Experimentally obtained magnetic properties for several ranges of doping suggest a competitive mixing of ferrimagnetic and ferromagnetic behaviors within the sample. The segregated phase for higher percentage of doping has also been identified.

DOI: 10.1103/PhysRevB.81.184421 PACS number(s): 75.50.Pp, 75.60.−d, 71.20.−b

I. INTRODUCTION

ZnO, a wide band gap, n-type semiconducting optoelectronic material received renewed interest both experimentally as well as theoretically following the suggestion by Dietl *et al.*[1] and Ueda *et al.*[2] based on a theoretical calculation that transition-metal (TM)-doped ZnO may be a possible diluted magnetic semiconductor (DMS) for room-temperature spintronic applications. This prediction resulted in intense experimental activity to realize room-temperature ferromagnetism in TM-doped ZnO. However, the experimental results on room-temperature ferromagnetism are highly controversial and the success in obtaining magnetism primarily depends on the details of the method employed for sample preparation.[3–5] Among the various singly doped ZnO systems, Fe-doped[6] and Co-doped ZnO (Refs. 3, 4, and 7–10) have *often* been observed to be ferromagnetic in bulk, thin films, as well as in nanophase. Recently Fe-doped ZnO nanocrystals[6] were found to be ferromagnetic with high Curie temperature. Local magnetic probes like electron paramagnetic resonance and Mössbauer spectroscopy indicate the presence of Fe in both valence states Fe^{2+} and Fe^{3+} and this coexistence is found to be important for obtaining ferromagnetic ordering in this material. The presence of Fe^{3+} was attributed to the possible hole doping in the system by cation (Zn) vacancies suggesting the crucial role of defects to promote ferromagnetism in these systems. The theoretical investigations by Chanier *et al.*[11] have also shown that for ZnO system, the favorable magnetic state in presence of a neutral cation vacancy is a spin-triplet ferromagnetic state, whereas anionic vacancy leads to a spin-singlet antiferromagnetic state. For substitutional Co dopant, on the other hand, proximity of surface[10] or electron doping in presence of O vacancies[12] is seen to enhance the magnetization of the system. In a detailed experimental observation, presence of Co interstitials are also seen to be effective in mediating long-range ferromagnetic order in Co-doped ZnO system.[4] There are also recent evidences about the tendency of substitutional Co ion to form a ferromagnetic cluster.[13]

Despite this experimental success, the theoretical studies based on density-functional theory within local spin-density approximation (LSDA)+Hubbard U predict an antiferromagnetic insulating ground state for Fe and Co singly doped systems.[14,15] In case of Fe-doped ZnO, presence of anionic and cationic vacancies are known to have significant effects on the carrier density and hence on the magnetic properties. Theoretical analysis reveals that for obtaining long-range half-metallic ferromagnetism, Zn vacancy is more crucial than O vacancy.[5,6]

Codoping, i.e., doping ZnO simultaneously with two different (suitably chosen) TM impurities has been another route to achieve ferromagnetism. Codoping the ZnO system with shallow acceptors and donors has been used to adjust

the carrier density of the system such that it can switch from the diluted magnetic insulator (DMI) to DMS behavior. Explanation toward the ferromagnetic behavior in DMI and DMS phases are given in terms of bound magnetic polarons[16–19] and carrier-mediated exchange,[20,21] respectively. Recent studies on (Ga,Co)-codoped ZnO show the role of octahedral interstitial Ga ion and O vacancies in mediating room-temperature ferromagnetism in this material.[22] Nonmagnetic Co-doped ZnO are also seen to have ferromagnetic behavior when codoped with Li.[23] On the other hand, codoping with Al leads to contradicting experimental results for Co-doped ZnO.[24,25] The (Co,Cu)-codoped ZnO system is seen to be ferromagnetic.[26,27] The (Fe,Co)-codoped systems, in particular, have been investigated in bulk, thin film[28] as well as in nanorods.[24] While the bulk behaves as an antiferromagnetic insulator,[27] both the thin film as well as nanorods show ferromagnetism with a reasonably high transition temperature.[24,28]

Motivated by the above theoretical and experimental observations, we have studied in some details the (Fe,Co)-codoped ZnO system, both theoretically and experimentally. Electronic structure calculation for (Fe,Co)-codoped ZnO has been carried out for bulk and ZnO cluster, both in the absence as well as in the presence of defects like O (V_O) and Zn vacancies (V_{Zn}). Our calculations for bulk as well as for cluster indicate the crucial role of defects for promoting magnetism in the codoped system. In practice, nanocrystalline systems are more prone to defects. So, in our experimental studies, we have investigated the (Fe,Co)-codoped nanocrystalline systems with varying percentages of codoping and studied the magnetic behavior of these systems with low-temperature magnetization and electron paramagnetic resonance (EPR) measurements. The experimental results corroborate our theoretical studies. Moreover, in ZnO-based DMO systems, presence of segregated phases for higher percentage of TM doping is an interesting issue. In order to elucidate this impurity phase, we have carried out studies on magnetic properties for a sample with higher percentage of codoping.

The remainder of the paper is organized as follows. In Sec. II, we have described the computational details and theoretical results calculated within DFT+U approach in case of bulk and cluster Fe-Co-codoped ZnO system in two different sections. Section III gives a detailed description of experimental studies. The last section summarizes the results with a conclusion.

II. COMPUTATIONAL DETAILS AND THEORETICAL RESULTS

A. Bulk-codoped system

Pure ZnO, in its wurtzite bulk structure, the hexagonal analog of zinc-blende lattice, belongs to the space group $P6_3mc$ with two formula units per unit cell. In order to simulate the systems with varying TM-dopant concentration, we have constructed a $(2\times2\times2)$ supercell consisting of 32 atoms from the wurtzite ZnO, so that replacing one Zn by a TM ion is equivalent to a concentration of 6.25%. We have investigated the electronic structure and the resulting magnetic properties of (Fe,Co)-codoped ZnO system with the help of linear muffin-tin orbitals method in the atomic sphere approximation,[29,30] with combined correction terms, within the framework of LSDA+Hubbard U approach. The Hubbard U is added explicitly to the LSDA Hamiltonian using the methodology prescribed by Czyzyk and Sawatzky.[31] For the exchange correlation potential, we have used Perdew-Wang parametrization.[32] Self-consistency is achieved by performing calculations on a $16\times16\times16$ k mesh for the Brillouin zone integration. The on-site d-d Coulomb interaction, U and the on-site exchange interaction, J applied to the d orbital of the TM ions are taken to be 5 eV and 1 eV, respectively, for all of our bulk calculations.

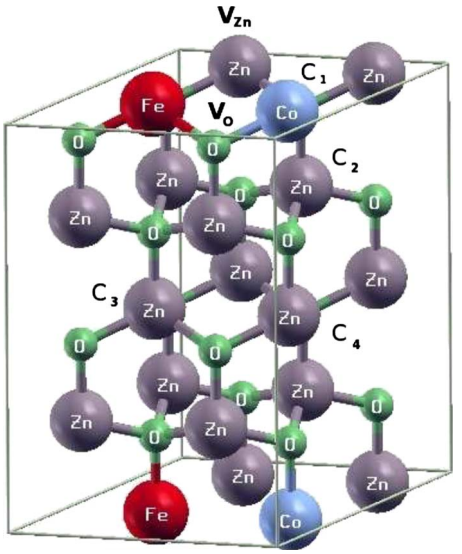

FIG. 1. (Color online) Part of the hexagonal wurtzite structure of ZnO is represented with Fe and Co ions substituting the upper plane Zn atoms. The Zn-vacancy (V_{Zn}) and O-vacancy (V_O) positions are shown in the figure. Also, four different configurations with varying Co-ion positions replacing Zn are depicted in the figure by C_1, C_2, C_3, and C_4, respectively (see Sec. II A 4 for more detailed description).

In this section, we shall present the results for Fe- and Co-codoped ZnO bulk system, where we have substituted two Zn atoms by one Fe and one Co atom, under three different situations, viz., (i) without any defect (vacancy), (ii) with an oxygen vacancy (V_O), and (iii) with a Zn vacancy (V_{Zn}). Percentage of V_O and V_{Zn} is equal to the TM-dopant concentrations in the supercell. The structural details of the supercell with TM-dopant positions are shown in Fig. 1. Presence of vacancies is simulated by replacing the respective inequivalent ion with an empty sphere of the same radius. The V_O are located at the first-nearest-neighbor inequivalent position from the dopant TM atoms while the V_{Zn} positions are chosen to be at the same plane as the TM dopants as shown in Fig. 1. In order to investigate the nature of exchange, we have done the calculation with varying distance between the TM dopants and compared the energies in parallel and antiparallel spin configurations. In the following we discuss each of these three cases along with their intercomparison.

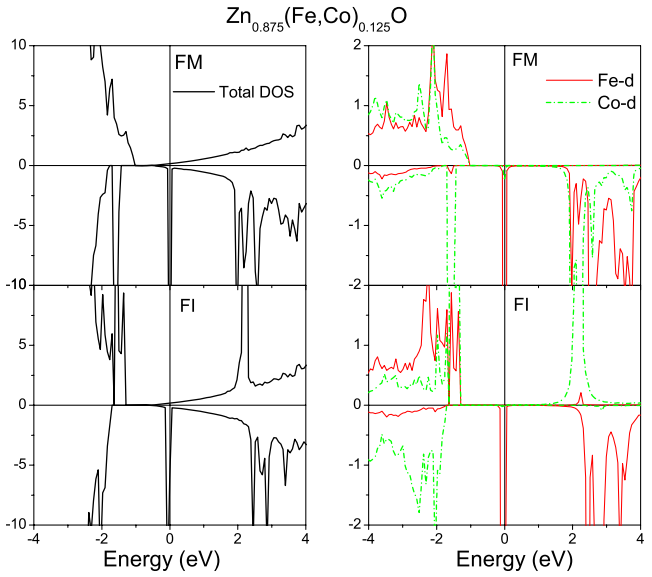

FIG. 2. (Color online) The left and the right panels of upper and lower rows present, respectively, the total and site-projected DOS from LSDA+U calculations for the $Zn_{0.875}(Fe_{0.5},Co_{0.5})_{0.125}O$ system. The upper and the lower panels of each figure represent the DOS for FM and FI configurations, respectively. In the partial DOS plots, the Fe and Co-d states are drawn by (red) solid and (green) dashed-dotted lines, respectively.

1. Case I: $Zn_{0.875}(Fe_{0.5},Co_{0.5})_{0.125}O$ *system*

In Fig. 2 we present the LSDA+U density of states (DOS) for (Fe,Co)-codoped ZnO with Fe and Co moments parallel [ferromagnetic (FM)] and antiparallel [ferrimagnetic (FI)] to each other. While the left panel of each figure shows the total DOS, the right panel display Fe-d and Co-d partial DOS for FM and FI configurations. Without any defects in the pristine ZnO system, the d levels of Fe and Co ions (separated by a distance 3.25 Å) in a tetrahedrally symmetric crystal field are split into twofold and threefold degenerate e and t_2 states, respectively, with the e states being lower energetically. Considering the TM ions to have only substitutional occupancy at the Zn site, the oxidation state of both the dopants is expected to be 2+. In the spin-polarized condition, the system favors a high-spin configuration, where for Fe, in the d^6 configuration, the majority spin (spin-up) channel is completely filled $[d\uparrow(5)]$ and the minority spin channel $e\downarrow(1)$ is half filled. For Co in d^7 configuration, in a similar way, $d\uparrow(5)e\downarrow(2)$ are completely filled. The FM DOS and partial DOS presented in Fig. 2 precisely reflect the above-mentioned distribution of electrons. As expected, in the FI state the occupancies of Fe and Co for up and down spin channels are reversed, where we have $d\uparrow(5)e\downarrow(1)$ for Fe while $d\downarrow(5)e\uparrow(2)$ for Co. It is interesting to note that Fe-e states remain half filled even in the presence of U as the LSDA+U method, which is designed to make the configuration with larger magnetization more favorable is not effective here, since it involves degenerate bands of only one spin channel, while the double counting correction remains operative. The FI state is more stable than the FM state and the energy difference is calculated to be 68.5 meV. In Table I, the average spin magnetic moments per ion and the total moment are listed for FM and FI states. Similar to the observations made in previous works by Park and Min[27] and Gopal and Spaldin,[14] we find that there is very little hybridization-induced charge transfer between the two TM d states. The spin-only magnetic moment for this systems is expected to be $7\mu_B$ and $1\mu_B$ for FM and FI arrangements of spins, respectively, while the individual moments for Fe and Co ions are $4\mu_B$ and $3\mu_B$, respectively. The calculated magnetic moments are consistent with the above picture.

The interplay of magnetism and electronic structure of the system is expected to change drastically with n-type or p-type doping introduced in the presence of oxygen vacancy (V_O) or zinc vacancy (V_{Zn}), respectively, which we consider next.

2. Case II: $Zn_{0.875}(Fe_{0.5},Co_{0.5})_{0.125}O+V_O$ *system*

The presence of an V_O provides n-type carriers within the system where each V_O will leave behind two electrons in the system. These carriers, if uniformly distributed over the partially filled minority d states of the TM dopants, the electronic configuration of Fe and Co ions will be d^7 and d^8, respectively, resulting in $e\downarrow(2)$ is fully filled for Fe and $t_2\downarrow(1)$ is one-third filled for Co. However, these extra carriers are mostly delocalized and depending on the proximity of the V_O to the TM dopants, these delocalized states selectively hybridize the respective TM-d states. From Fig. 3 we

TABLE I. The average magnetic moments (in μ_B) per ion for FM and FI configurations in (Fe,Co)-codoped ZnO in absence and presence of vacancy (V_O and V_{Zn}) as derived from LSDA+U calculations.

	Ferromagnetic configuration			Ferrimagnetic configuration		
Ion	No vacancy	O vacancy	Zn vacancy	No vacancy	O vacancy	Zn vacancy
Fe	3.667	3.607	4.009	3.662	3.585	4.078
Co	2.651	2.512	2.664	−2.633	−2.629	−2.610
Zn	0.003	0.004	0.013	0.001	0.000	0.0098
O	0.025	0.026	0.110	0.001	−0.002	0.084
V_O		0.202			0.043	
V_{Zn}			0.198			0.032
Total	6.974	6.783	8.89	1.069	0.97	2.97

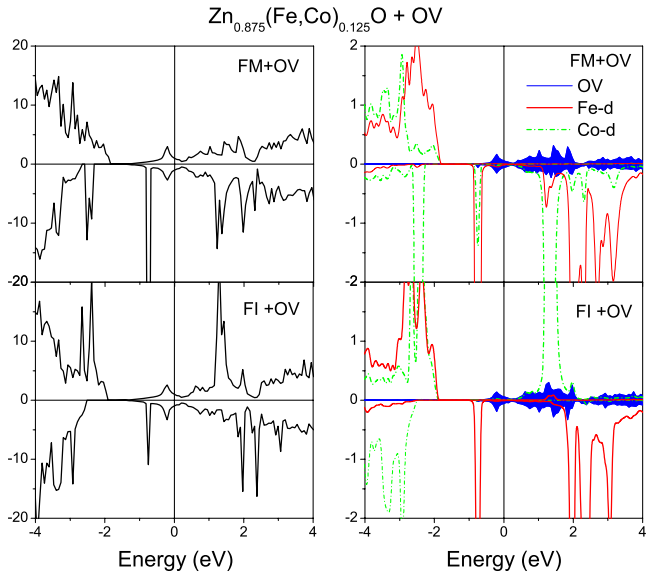

FIG. 3. (Color online) The left and the right panels of upper and lower rows present, respectively, the total and site-projected DOS from LSDA+U calculations for the $Zn_{0.875}(Fe_{0.5},Co_{0.5})_{0.125}O+V_O$ system. The upper and the lower panels of each figure represent the DOS for FM and FI configurations, respectively. In the partial DOS plots, the Fe and Co-d states are drawn by (red) solid and (green) dashed-dotted lines, respectively. V_O PDOS is shown by filled (blue) curve.

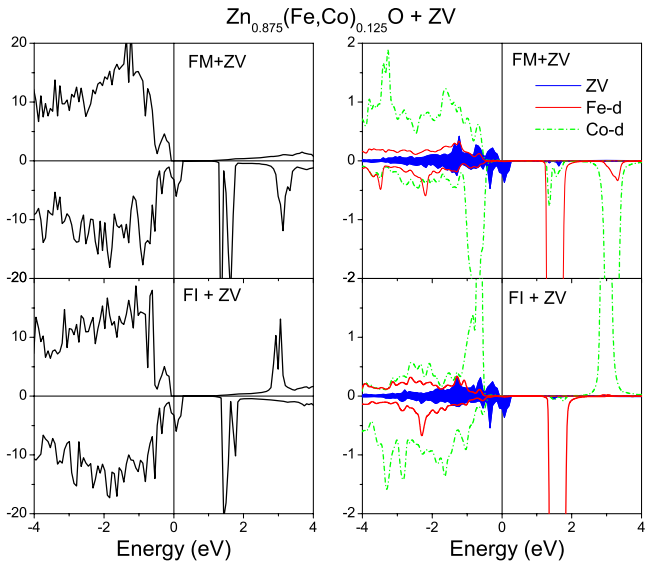

FIG. 4. (Color online) The left and the right panels of upper and lower rows present, respectively, the total and site-projected DOS from LSDA+U calculations for the $Zn_{0.875}(Fe_{0.5},Co_{0.5})_{0.125}O+V_{Zn}$ system. The upper and the lower panels of each figure represent the DOS for FM and FI configurations, respectively. In the partial DOS plots, the Fe and Co-d states are drawn by (red) solid and (green) dashed-dotted lines, respectively. V_{Zn} PDOS are plotted with filled (blue) curve.

gather that, in presence of V_O, while $e\downarrow(2)$ is completely occupied for Fe,Co $t_2\downarrow$ states are hardly filled. The Fermi level is dominated by delocalized vacancy-induced states which introduce metallicity into the system and at E_F, there are no TM-d states. The FI state is found to be energetically stable with an energy difference calculated to be 73.5 meV. Table I lists the average spin-only magnetic moments for all ions and the V_O in the supercell in FM and FI configurations. From the table we gather that Fe and Co moments reduce slightly as the minority states are more occupied and also the vacancy derived states now acquire a finite magnetic moment.

3. *Case III:* $Zn_{0.875}(Fe_{0.5},Co_{0.5})_{0.125}O+V_{Zn}$ *system*

In presence of a single V_{Zn}, the system is doped with two p-type carriers (holes). We gather from Fig. 4 that on introduction of V_{Zn}, Fe $e\downarrow$ is unoccupied and there is a localized shallow acceptor level introduced by V_{Zn} state admixed with half-filled Co-$e\downarrow(1)$ state. As a result Fe moment increases and the vacancy-derived state also acquires appreciable moment, as can be seen in Table I. Under the framework of LSDA+U, this system stabilizes in a FI-half-metallic state with an energy difference of 97.7 meV with the FM configuration. The resulting half metallicity is due to the localized V_{Zn}-induced states at E_F.

It is interesting to note that in the presence of vacancies, the extra carriers introduced into the system primarily affect the occupancy of the minority Fe-d states, while Co occupancy is hardly affected, since the moment of the Co ion, as reflected in Table I, is almost the same for all the cases. Further, antiparallel alignment of spins is found to be stable for all the three cases under LSDA+U.

4. *Comparison of these three cases*

Next, we consider four different configurations (C_1, C_2, C_3, and C_4), for all the three cases considered, for four different separations (in increasing order) between the two TM ions and calculate the energy differences between FI and FM cases [Δ (ferri-ferro)] both within LSDA and LSDA+U, which are plotted in Fig. 5 left and right panels, respectively. These plots are suggestive about the type of the magnetic exchange interaction. From Fig. 5 we find that for the case I (without any defect) and case III (with V_{Zn}) within LSDA the sign of the exchange integral switches from FI to FM with the change in the distance between the dopant TM ions. This is very similar to Ruderman, Kittel, Kasuya, Yoshida (RKKY)-type exchange interaction as suggested by Park and Min[27]and Lathiotakis *et al.*[26] However, for case II (with V_O) the exchange interaction always remains ferromagnetic within LSDA while its magnitude alternatively change from one configuration to the other.

The results are quite different when the calculations are carried out in the framework of LSDA+U. With application of U, the fluctuating RKKY-type magnetic exchange changes into a competitive behavior between parallel (double-exchange) versus antiparallel (superexchange) configurations of Fe and Co spins. This kind of competition between parallel (FM) and antiparallel (FI) spin orientations is quite common in case of TM-doped ZnO systems.[6,15] The exact exchange behavior depends on the distance between the TM dopants and position of vacancies with respect to the dopant

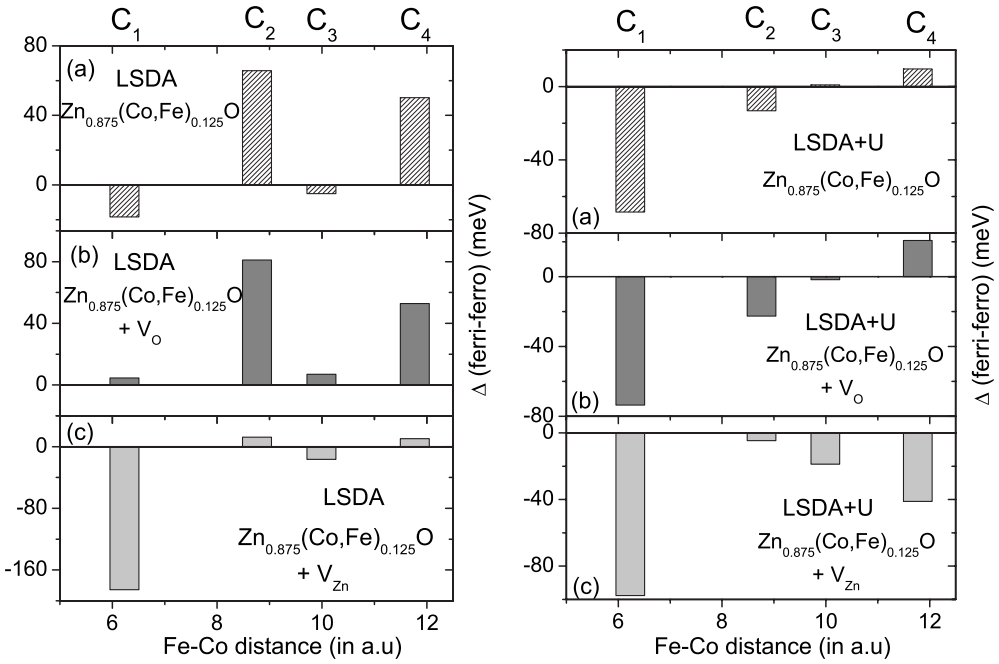

FIG. 5. The left panel of the figure depicts the energy difference between FI and FM configurations as calculated within LSDA with varying distances (in a.u.) between a Fe and Co ion pair. Four different positions with increasing distance between the two ions are denoted as C_1, C_2, C_3, and C_4, respectively. The results are plotted for the three cases (I, II, and III). In the right panel, similar energy differences are plotted for LSDA+U calculation.

positions. For all the three cases, as shown in the right panel of Fig. 5, the exchange interactions are seen to be primarily ferrimagnetic. Only at large distance between dopant TM ions, for the case I (no defect) and case II (with V_O), ferromagnetism wins.

We would like to mention here about the nature of exchange interactions for a smaller ($2\times2\times1$) supercell with larger percentage (12.5%) of TM dopants. Within LSDA, for cases I and II, the exchange mechanism is RKKY type. Case III remains in FI state for all four configurations. However, with LSDA+U, case I stabilizes in FI state, case II continues the RKKY-type exchange behavior, and, most surprisingly, case III stabilizes in FM state for all four configurations. This stabilization of FM state is related with the less-localized (in comparison to the $2\times2\times2$ supercell) nature of V_{Zn} states, which may take part in mediating the FM-long-range order.

Recent experimental studies[13,25] have shown that for Co-doped ZnO system, there is a tendency of substitutional Co ions to form ferromagnetic clusters. Keeping this fact in mind, we tried to find out the exchange mechanism of a codoped system where, the exchange behavior of a pair of Co ions is studied in presence of a Fe ion at a nearest-neighbor position both with and without vacancies. The exchange interactions are calculated as a function of the separation between two Co ions with two different positions of O and Zn vacancies. The V_O positions are defined as near and far depending on the position of the V_O with respect to the Co pair. The V_{Zn} are kept on the in-plane and out-of-plane positions. In Fig. 6, the energy difference as obtained from an LSDA+U calculation between antiferromagnetic (AFM) and FM configurations (Δ_{AFM-FM}) of the two Co ions is plotted with varying distances between the two Co ions. It is evident from the figure that for first and second nn positions of the two Co ions, the system tends to stabilize in a ferromagnetic ground state for almost all the configurations (except out-of-plane V_{Zn}) considered here, which implies that in presence of a Fe as codopant, the exchange behavior of Co ions is mostly ferromagnetic.

Our calculations of the preceding section reveal that ferrimagnetic state is favorable in the (Fe,Co)-codoped bulk ZnO, even in the presence of defects. As we have discussed

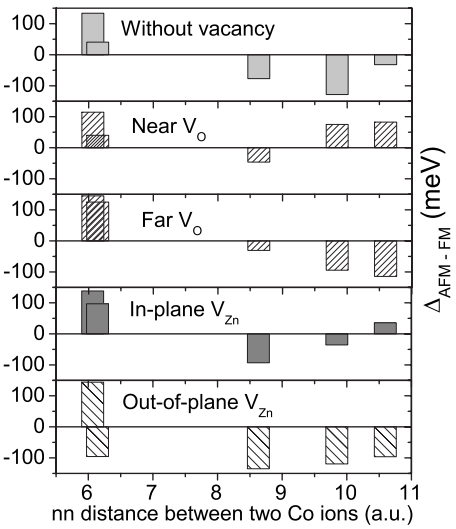

FIG. 6. The figure depicts the energy difference between AFM and FM configurations of a pair of Co ions in presence of a nearest-neighbor Fe ion in various possible cases, viz., without any vacancy, near V_O position, far V_O position, in-plane V_{Zn} position, and out-of-plane V_{Zn} position.

earlier, it has been possible to successfully dope Co and Fe in ZnO nanosystems, where the surface is found to play a key role to promote magnetism. To understand the effect of surface on the magnetic properties of nanosystems in detail, we have studied the electronic structure of a small ZnO cluster upon codoping with Fe and Co. In the following we shall present the results of codoping Fe and Co in ZnO cluster and compare the results with the bulk calculations.

B. Co-doped $Zn_{12}O_{12}$ cluster

The study of codoping Fe and Co in the ZnO cluster was carried out in the framework of generalized gradient approximation (GGA) (Ref. 33) plus Hubbard U (GGA+U) method,[34] as implemented in the VASP (Refs. 35 and 36) code. The onsite Coulomb interaction strength (U) was taken to be 4 eV and the on-site exchange interaction strength (J) was taken to be 1 eV, as this choice of values was found to yield reasonable results for ZnO clusters doped with TMs and also very close to the values chosen for our studies on bulk ZnO. We have used the projector augmented wave[37] method along with plane-wave basis set. The plane-wave energy cutoff is taken to be 500 eV. Only one k point (Γ point) was used for all the calculations with clusters. The atomic positions are relaxed to minimize the Hellman-Feynman force on each atom with the tolerance value of 0.01 eV/Å.

To identify the stable defect states in codoped ZnO cluster, we have calculated the formation energies (FEs) corresponding to defects like Zn vacancy and O vacancy in different charge states. The expression for the calculations of the formation energies is:[38] $\mathrm{FE}=E[\mathrm{Zn_mO_n}(\alpha,q)]-E[\mathrm{Zn_pO_p(pure)}]+\Sigma_\alpha n_\alpha\mu_\alpha+q(E_v+\epsilon_F)$, where α is the defect atom added to or removed from the pristine ZnO cluster, n_α is the number of each defect atom: $n_\alpha=-1(+1)$ for adding (removing) *one* atom, $E[\mathrm{Zn_mO_n}(\alpha,q)]$ is the total energy with defect α and charge q, while $E[\mathrm{Zn_pO_p(pure)}]$ is the total energy of pure ZnO cluster. ϵ_F is the Fermi level measured with respect to the energy (E_v) of the highest occupied molecular orbital (HOMO) in pristine ZnO cluster. μ_α is the chemical potential of atom α in some suitable reservoir.

Chemical potentials of Zn and O can vary in a range keeping the ZnO cluster stable and satisfying the condition: $p(\mu_{\mathrm{Zn}}+\mu_{\mathrm{O}})=E[\mathrm{Zn_pO_p(pure)}]$, where p is the number of ZnO units in the cluster. Thus, there is only one free parameter between μ_{Zn} and μ_{O}. The limits where μ_{O} has the maximum and minimum allowed values are called the oxygen-rich limit and oxygen-poor limits, respectively.

We have considered codoping of Fe and Co by substitution of two Zn atoms of the stable $Zn_{12}O_{12}$ cluster. The cluster has a shape of hollow sphere with the diameter of ~6.35 Å. The cluster of this size is very stable (magic-sized cluster)[39] and all the atoms are located on the surface of a sphere in this cluster, providing an unique opportunity to study the surface contribution to magnetism in ZnO nanoparticles. Further, doping of TM has been extensively studied theoretically in such a cluster.[38] In our study of defects, we have concentrated on Zn and O vacancies in different charge states as these are reported to be the most relevant defects in ZnO.[40] The formation energies are calculated for ZnO clusters doped with Fe and Co at different charge states in the absence as well as in the presence of the vacancies. The results of the calculations are displayed in Fig. 7. Since the oxygen-rich limit gives higher stability (lower formation energy) to the system, so in Fig. 7 we have shown the results in the O-rich limit only. We note from the figure, as expected in the oxygen-rich limit, the formation of oxygen vacancy is not energetically favorable. The stable charge states of the codoped cluster without vacancy are 0 and +1. Charge states 0 and −1 become the stable states in the presence of Zn vacancy. Overall, in the absence of vacancy, +1 charge state (at the p-type region) and the neutral state are the most stable states, however, −1 charge state in the presence of Zn vacancy becomes the most stable states at n-type region. This observation is in agreement with the reports on single TM-doped ZnO clusters.[38]

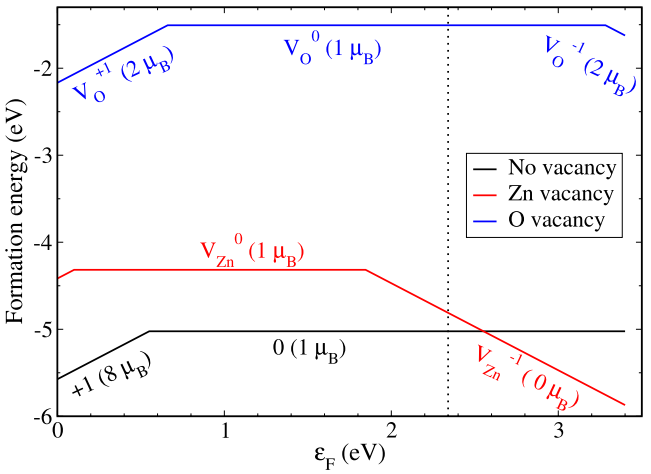

FIG. 7. (Color online) Formation energies in the oxygen-rich limit for codoped ZnO cluster at different charge states in the absence as well as in the presence of vacancies. Only the stable part of a certain charge state is shown. The Fermi energy (ϵ_F) has been varied up to the experimental band gap of bulk ZnO and the dotted vertical line indicates the HOMO-lowest unoccupied molecular orbital gap of the pristine ZnO cluster.

After identifying the stable defect states in codoped ZnO cluster, we have calculated the difference in energy between the antiparallel and the parallel spin arrangements of the TM ions for the stable charge states, as shown in Fig. 8. From this figure, it is interesting to note that the parallel spin alignment (FM) is favored in the charge state +1 in the absence of vacancy, leading to ferromagnetic tendency in the cluster. This also points to the fact that the TM ions may be in 3+ oxidation state, as evidenced in the Fe-doped ZnO cluster.[38] For all the other stable states, the antiparallel alignment is favored, leading to ferrimagnetism. This observation is in good agreement with the LSDA+U results for codoped bulk ZnO, described in the previous section, suggesting antiparallel arrangement of spins is preferred in Fe-Co codoped ZnO, even in the presence of defects.

III. EXPERIMENTAL OBSERVATION

For a systematic investigation of the magnetic properties of (Fe,Co)ZnO systems, we have prepared nanocrystalline

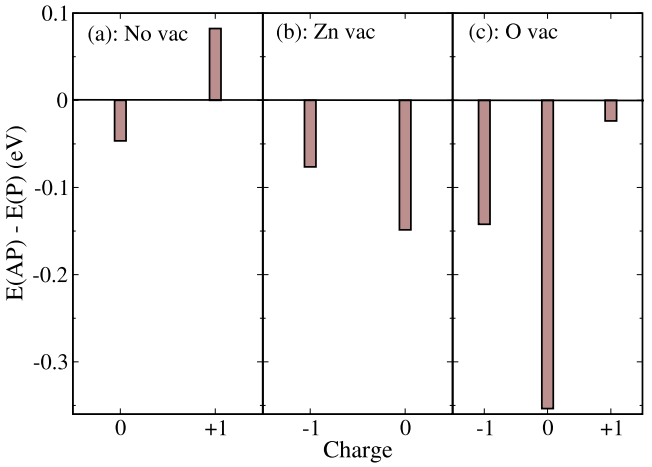

FIG. 8. (Color online) The difference in energy between the antiparallel and the parallel spin arrangements of the TM ions for the stable charge states with (a): no vacancy, (b): V_{Zn}, and (c): V_O.

codoped ZnO, the codoping percentage being 5%, 10%, and 15% for each of the TM dopants. For higher percentage of TM dopant in ZnO, there are earlier evidences[41,42] of segregating into spinel ferrite phases. For that purpose, we have also investigated one sample with higher percentage (15% Fe, 15% Co) of doping in a detailed manner.

A. Sample preparation and structural characterization

Nanocrystalline powders of (Fe,Co)ZnO samples are prepared by chemical pyrophoric reaction method. Depending on the percentage of TM doping, required amount of $Zn(NO_3)_2 \cdot 6H_2O$, $Co(NO_3)_2 \cdot 6H_2O$, and $Fe(NO_3)_3 \cdot 9H_2O$ are dissolved in distilled water. This solution was heated at 190 °C with constant stirring and triethanol amine is subsequently added in a ratio 4:1 with the metal ions in order to precipitate them with amine. At the same temperature HNO_3 is added to dissolve the precipitate and the resulting clear solution was evaporated with constant stirring at the same temperature. After complete dehydration, the obtained precursor powder was ground and calcined at 350 °C. The calcination temperature is optimized to avoid any secondary phase formation. TEM image of $Zn_{0.9}(Fe_{0.5}Co_{0.5})_{0.1}O$ sample in Fig. 9 confirms the nanocrystalline nature of the sample. In Fig. 9(a), the low-magnification bright-field TEM micrograph shows a broad particle-size distribution present in the sample with an average size of 7–8 nm. Figure 9(c) presents the high-resolution TEM micrograph indicating that the nanoparticles are single crystalline in nature. In Fig. 9(b), the selected area diffraction (SAD) pattern, with an electron beam of 20 nm diameter, confirms the crystallinity and preferential orientation of each nanoparticle. Figure 10 depicts the powder x-ray diffraction (XRD) patterns for the three samples $Zn_{0.9}(Fe_{0.5}Co_{0.5})_{0.1}O$, $Zn_{0.8}(Fe_{0.5}Co_{0.5})_{0.2}O$, and $Zn_{0.7}(Fe_{0.5}Co_{0.5})_{0.3}O$. From now onwards in this paper, we shall designate these three samples as samples 1, 2, and 3, respectively. There are clear evidences of secondary phases in the XRD pattern of sample 3 as indicated by the arrows. All experimental data for sample 3 will be described in detail

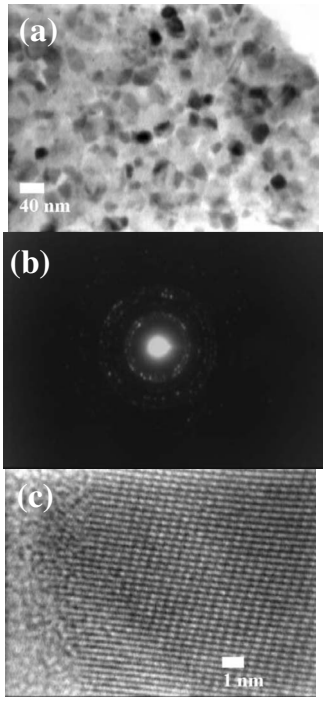

FIG. 9. (a) Low-magnification bright-field TEM micrograph for sample 1(see text). (b) SAD pattern showing the single-crystalline nature of the sample. (c) High-resolution TEM micrograph implying the nanocrystallinity.

in a separate Sec. III D. Figure 11 shows the Le-Bail profile-fitted data for sample 1. The cell parameters derived from the profile fitting are a=3.2511(3) Å and c=5.2022(5) Å, respectively. In the same figure, we also show the Cu-$K\alpha$ line

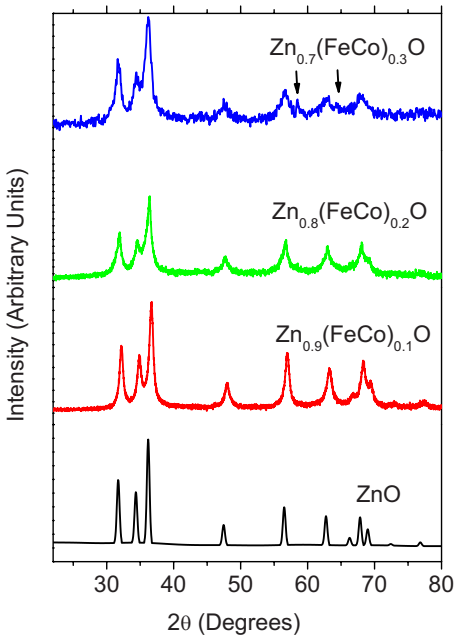

FIG. 10. (Color online) Experimental XRD data for pure ZnO nanocrystalline sample and data for the three samples (see text) are plotted. Sample having highest doping percentage shows presence of impurity phases in the XRD plot (as shown by arrow marks).

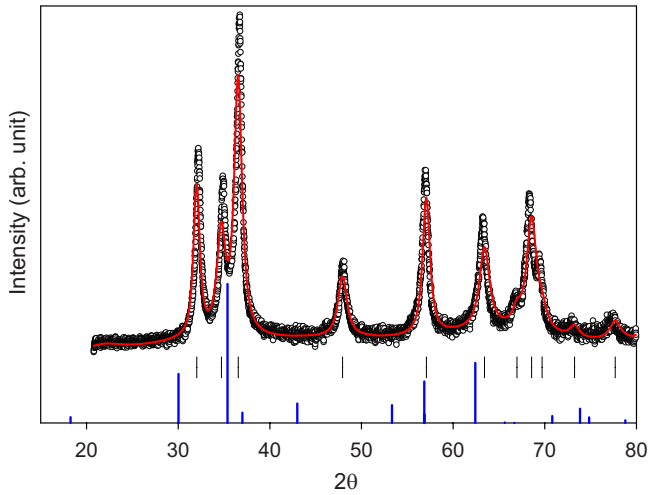

FIG. 11. (Color online) Le-Bail-fitted XRD data for nanocrystalline sample $Zn_{0.9}(Fe_{0.5}Co_{0.5})_{0.1}O$. The open circles represent the experimental data, red line is the fit, and the blue lines below represent the Cu-$K\alpha$ line positions for spinel-ferrite system as described in Sec. IV. The lattice parameters extracted from fitting are given in text.

positions [by vertical (blue) lines on the x axis] for the spinel-ferrite system, which is the most commonly suspected segregated phase for such systems.[41,42] These line positions indicate that in sample 1, XRD does not show any clear evidence of phase segregation, although the small minor peaks from spinel phase may be hidden within the background noise. Also, we cannot conclude about the presence of very small quantity of Fe and Co nanoclusters within the sample from XRD data. However, successive EPR measurements nullify the presence of any such secondary phases within the sample with lower concentration of codopants. For sample 3, comparison of ferrite line position with the impurity lines (shown by arrow marks in Fig. 10) shows that the segregated phase may be spinel ferrite. We will again discuss this fact in detail in Sec. III D. Increasing dopant concentration leads to a decrease in crystalline correlation and thereby an increase in the XRD peak widths. The structural characterization has been carried out using a standard x-ray diffractometer (Phillips, PW-1729) with monochromatic Cu $K\alpha$ radiation and by a high-resolution transmission microscope (JEOL, JEM-2010, 200 kV).

B. Magnetization measurements

We have investigated the bulk magnetic properties of all these three samples with a Quantum Design Magnetic Property Measurement System (MPMS) superconducting quantum interference device and the local magnetic properties with EPR. The left upper panel of Fig. 12 shows the temperature dependence of magnetization of sample 1 in both zero-field-cooled (ZFC) and field-cooled (FC) conditions for the applied field value $H=200$ Oe from 5 to 300 K. The concave nature of the magnetization curve indicates a carrier-mediated magnetic behavior with low carrier density and localized nature of the carriers for such systems.[18] With increasing dopant concentration, the concave nature of magnetization decreases indicating the increase in carrier density with dopant concentration. From the temperature dependence of magnetization data, irreversibility in magnetization seems to be present for a very small intermediate range of temperature for $H=200$ Oe. For an applied field value higher than the saturation magnetic field, ZFC and FC curve merges with each other. Left-lower panel of the same figure presents the calculated dc susceptibility obtained from the magnetization data of sample 1, clearly indicating a mixing of antiparallel (FI) $[C/(T+\theta)]$ and parallel-spin (FM) $[C/(T-\theta)]$ Curie-Weiss-type plots with $\theta\sim-50$ K (for FI) and 141 K (for FM), respectively, superposed over a paramagnetic Curie-type (C/T) background (indicated for sample 1, in Fig. 12, left lower panel). The right upper and lower panels display similar temperature-dependent magnetization and dc-susceptibility behavior for sample 2. The gross behavior remains almost similar except an increase in the temperature range of irreversiblity. Similar to sample 1, the dc susceptibility shows a mixed FI and FM behavior superposed over an underlying paramagnetic component. We shall discuss the magnetic behavior of sample 3 in the next section. Figure 13 represents the M vs H hysteresis loops at 5 and 300 K for sample 1 and 2. Inset of each figure shows the room-temperature hysteresis loop in a narrower field scale. For both of these samples, the little hysteresis present at 5 K almost disappears at room temperature. For such codoped

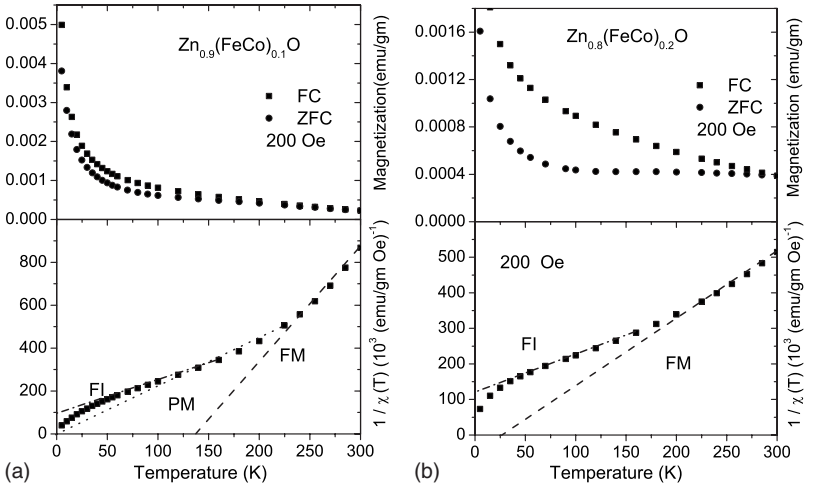

FIG. 12. The left and the right panels of the figure show the magnetization (M) vs temperature (T) behavior for ZFC and FC conditions of the samples 1 and 2, respectively (see text), with the applied field value of 200 Oe. In lower panel of each figure the $\frac{1}{\chi}$ vs T is plotted. The temperature dependence pattern of susceptibility shows the mixing of FI and FM within the system.

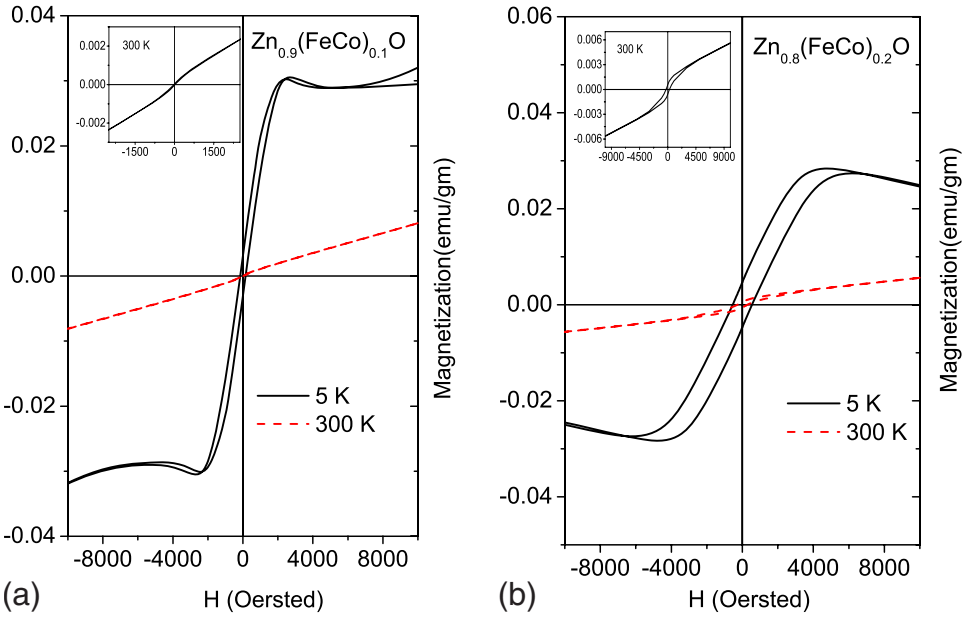

FIG. 13. (Color online) Hysteresis loops for samples 1 and 2 are plotted for the two temperatures (5 and 300 K). For samples with higher doping percentage, coercivity increases resulting in a larger loop area. The inset of both figures represents the room-temperature hysteresis behavior in a narrower field range.

system, an accurate determination of magnetic moment per Fe or Co ion is not possible. Hence we have calculated the average moment in Bohr magneton (μ_B) per TM ion. These low magnetic moments obtained from the magnetization measurements are presented in Table II.

C. EPR measurements

As a next step, to obtain a detailed microscopic information about the codoped system, EPR measurements were carried out for all these three samples. The EPR experiments were performed using a Bruker spectrometer at the X band (ν=9.60 GHz) equipped with 100 kHz frequency modulation. The temperature was varied from 105 to 300 K. Diphenyl-picrylhydrazyl was used as a reference for the calibration of g factors.

The EPR spectra for samples 1, 2, and 3 are plotted for comparison in Fig. 14 at two different temperatures, viz., 300 and 105 K. For plotting all three samples in the same scale in order to get a comparison of the evolution of spectra with temperature, intensities for samples 1 and 2 are multiplied by appropriate factors. In Fig. 14, the signals are presented as (A) 300 K and (B) 105 K for sample 1; (C) 300 K and (D) 105 K for sample 2; and (E) 300 K and (F) 105 K for sample 3. For both samples 2 and 3, the shoulderlike part (marked in Fig. 14) of the spectra at <500 G is a signature of the presence of spin-glass behavior,[43] which is encircled in the figure. For sample 1, with lowering of temperature, there is an increase in the intensity of EPR spectra with very small change in the line position. The evolution of spectra with temperature indicates a small ferromagnetic component su-

TABLE II. The average measured saturation magnetic moments (in μ_B/TM ions) for samples 1, 2, and 3 at H=10 000 Oe. With increasing dopant concentration, from sample 1 to sample 3, the average moment increases.

Temperature (K)	Sample 1	Sample 2	Sample 3
5	0.0473	0.0566	0.0685
300	0.0128	0.0132	0.0366

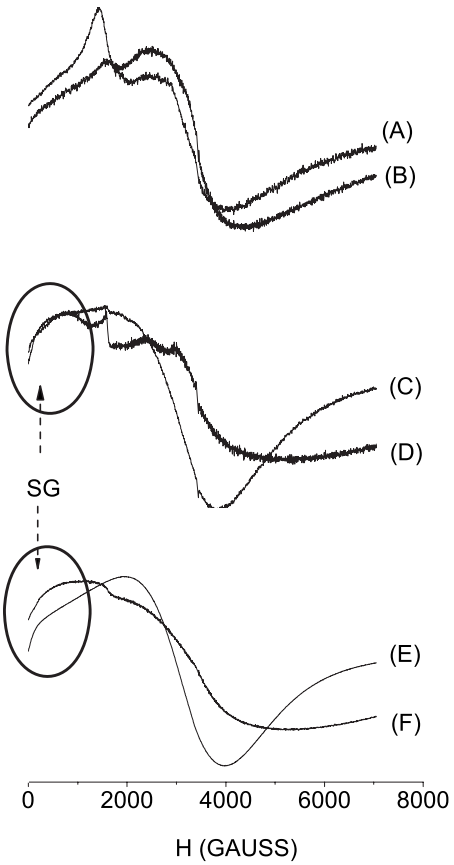

FIG. 14. The figure compares the EPR signals for the sample 1 at (a) 300 K and (b) 105 K, (c) 300 K; (d) 105 K for sample 2; and (e) 300 K and (f) 105 K for sample 3. Along y axis, the intensity of the EPR spectra is plotted in arbitrary units.

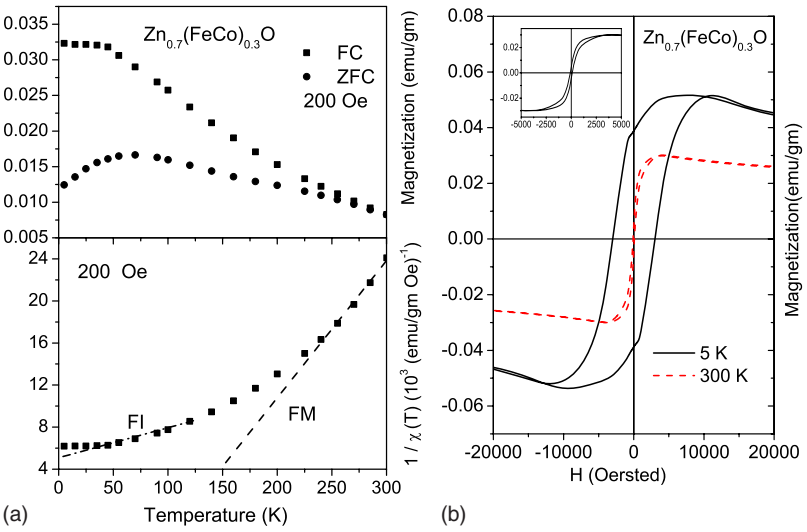

FIG. 15. (Color online) The M vs T (left panel) and M vs H (right panel) behaviors of sample 3 are plotted. The inset of the right panel shows the hysteresis behavior at room temperature in a narrower field range.

perimposed with a paramagnetic Curie-type background. The intense signal at ~3420 G is due to Fe^{3+} at Zn sites, whereas the weak shoulder at ~1520 G is due to Co^{2+} at Zn sites.[44,45] Presence of Fe^{2+} is difficult to resolve in the temperature range used in this study due to its short spin-lattice relaxation time. Presence of multiple valent state for Fe ion was observed in our earlier studies.[6,46] Also, the line-shape and resonant line-shift behaviors are different from the nanocrystalline Fe or Co systems,[47–49] indicating the absence of Fe or Co nanoclusters in the present system.

For samples 2 and 3, the temperature behavior of EPR line intensity is different from sample 1. With decreasing temperature, the line intensity initially increases and then decreases. Although the XRD and magnetization data of sample 2 is very similar to sample 1, EPR data of sample 2 are more close to the behavior of sample 3, where the presence of impurity phase is observed from XRD, as mentioned in Sec. III A. In the next section, we have shown a comparison of the temperature behavior of detailed EPR spectra of sample 1 (pure codoped sample) and sample 3(codoped sample with impurity phase) along with the magnetization results of sample 3. In the same section, we present some detailed investigation with the magnetization and EPR spectra of the predicted impurity phase.

D. Magnetic studies on sample 3: Impurity phase detection

For sample 3, having the largest concentration of the TM dopant, the M-T curve in the left upper panel of Fig. 15 shows a strong FM behavior with a low-temperature spin-glass phase. Presence of spin-glass behavior may be due to the canted surface spins of the nanoparticle system.[6] In the dc susceptibility plot in the left lower panel, however, a little admixture of FI component may be seen. In the right panel, the hysteresis behavior for sample 3 is plotted. It shows a large hysteresis loop and clear presence of FM behavior. However, we will now investigate whether the actual reason behind this FM behavior is due to the substitutional TM dopant or due to the presence of the impurity phase. In order to identify the impurity phase, we have also investigated $ZnFe_2O_4$ and Co-doped $ZnFe_2O_4$ nanoparticles, due to the evidence of the segregation of spinel-ferrite phase in doped ZnO in the literature.[41,42] It is observed that the M-T behavior and EPR data of sample 3 have more similarities with Co-doped $ZnFe_2O_4$, $Zn_{0.75}Co_{0.25}Fe_2O_4$. In Fig. 16, we have plotted the results of the structural and magnetic investigations on $Zn_{0.75}Co_{0.25}Fe_2O_4$. The profile-fitted XRD data are plotted for $Zn_{0.75}Co_{0.25}Fe_2O_4$ (Fig. 16, left panel) using Co-$K\alpha$ x ray. The lattice parameter $a=8.4086(8)$ Å is derived from the fitting for this cubic-spinel structure. We have used Co as a target for this particular sample to increase the signal-to-noise ratio. We may recall here that the impurity line positions of sample 3 (indicated by arrows in Fig. 10) matched with the Cu-$K\alpha$ line positions (indicated by blue lines in Fig. 11) of the spinel-ferrite phase. The magnetization (right top panel) and hysteresis (right-bottom panel) behaviors of $Zn_{0.75}Co_{0.25}Fe_2O_4$ are also plotted in Fig. 16. The M-T ZFC data show a spin-glass-type behavior and the hysteresis is mostly superparamagnetic due to the size effect in the nanocrystals. Although the M-T behavior of sample 3 is also having a low-temperature spin-glass phase, from the magnetization data, it is difficult to conclude about the partially segregated phase present in sample 3.

In order to elaborate the method of impurity phase detection, we have performed detailed EPR studies on (a) sample 1, where there is no evidence of segregated impurity phases (from XRD and TEM) and hence the signal comes only from substitutional dopants; (b) sample 3, where the effects of both substitutional dopants and segregated phase comes into play; and for (c) $Zn_{0.75}Co_{0.25}Fe_2O_4$, which represents the signal for the suspected impurity phase.

Figure 17(a) (left panel) presents the temperature dependence of the EPR spectra of sample 1 in the temperature range 110–300 K. With decreasing temperature, signal intensity monotonically increases and the line position shifts marginally for this sample indicating very less percentage of ferromagnetically coupled spins in this sample.

The middle panel of Fig. 17(b) depicts the temperature variation for sample 3. It may be mentioned that to record the EPR spectra for sample 3, the spectrometric settings were changed to a lower value of receiver gain (RG)$=1\times10^4$ and modulation amplitude (MA)$=1$ G (from RG$=4\times10^4$ and

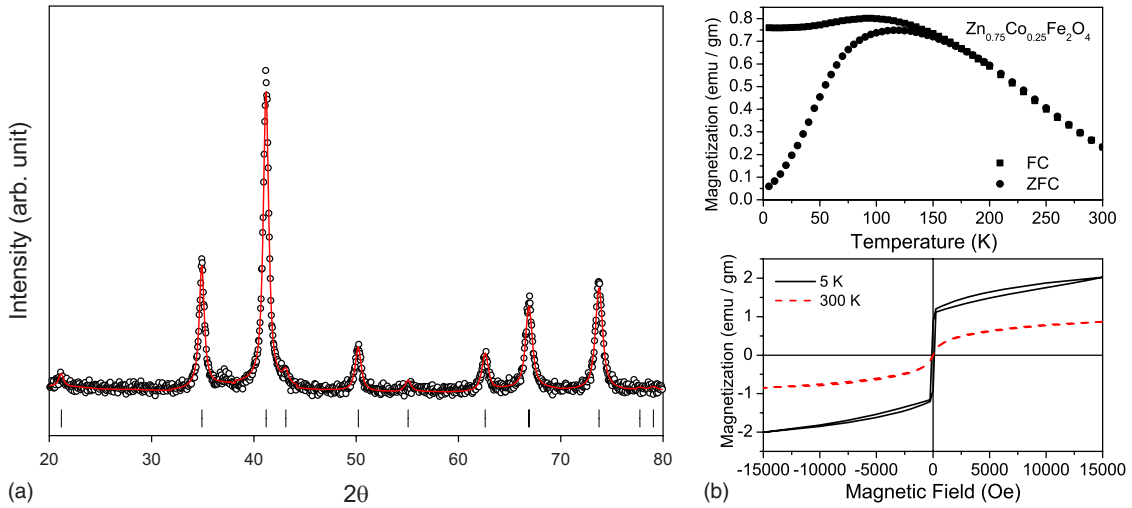

FIG. 16. (Color online) The Le-Bail profile fitted XRD data for $Zn_{0.75}Co_{0.25}Fe_2O_4$ are plotted using Co-$K\alpha$ x ray. M vs T (right-top panel) and M vs H (right-bottom panel) behaviors of the same sample are also plotted.

MA=1 G necessary for the other two samples), indicating the increase in ferromagnetic fraction in the sample with doping percentage. Here, as discussed in the previous section, with decrease in temperature, intensity of EPR signal initially increases and then reduces. In the same panel, the signal indicates (similar to the encircled spectra of Fig. 14) the presence of spin-glass phase in the system at low temperature, in accordance with the low-temperature ZFC magnetization data for the same sample. In addition to that, with lowering of temperature, there is a line-position shift toward lower field and increase in linewidth for the same sample.

The right panel of the Fig. 17(c) represents the evolution of the EPR signal of $Zn_{0.75}Co_{0.25}Fe_2O_4$ with temperature, where with decreasing temperature the intensity of the signal decreases monotonically. Also the presence of low-temperature spin-glass phase can be detected from the line shape indicated in figure.

Hence from Fig. 17, a qualitative observation of spectral behavior of sample 3, i.e., the initial increase in line intensity (similar to sample 1) followed by gradual decrease (similar to ferrite phase), indicates the presence of both the codoped phase and the ferrite-impurity phase in sample 3.

This qualitative observation becomes more clear from the resemblance of the detailed behavior of EPR signals for the ferrite-impurity phase and sample 3. The evolution of line position (H_r), linewidth (ΔH_{pp}), intensity of the EPR line and the area under the EPR line, providing a measure of the percentage of coupled spins, are plotted for sample 3 (middle panel) and the ferrite phase (right panel) in Fig. 18. For sample 1, the line position and linewidth of the EPR lines are also plotted for comparison in the same figure (left panel). Due to the complicated line shape for sample 1, calculation of intensity and area is not very accurate. Hence, we avoid plotting these quantities for sample 1. In sample 3, due to simultaneous presence of impurity phase along with Fe- and Co-codoped ZnO, the temperature evolution of the EPR signal will also have a mixed behavior, as can be seen from the comparison of line positions at the middle panel of Fig. 18. For the ferrite sample, the line position gradually shifts to a lower field value with decrease in temperature. For sample 3, although down to 200 K, the shifting of the line position toward lower field continues, with further lowering of temperature, the shift is toward higher field value, which is similar to the line position behavior for sample 1 (left panel).

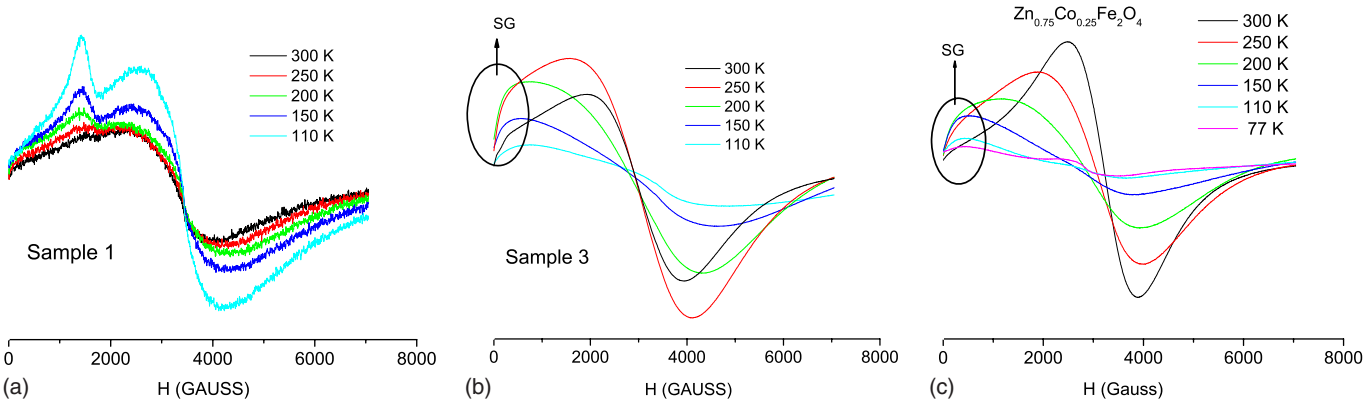

FIG. 17. (Color online) The left panel of the figure depicts the temperature variation in the EPR signal for sample 1, the same for sample 3 is plotted in the middle panel. Evolution of EPR signal for $Zn_{0.75}Co_{0.25}Fe_2O_4$ is shown in the right panel of the figure.

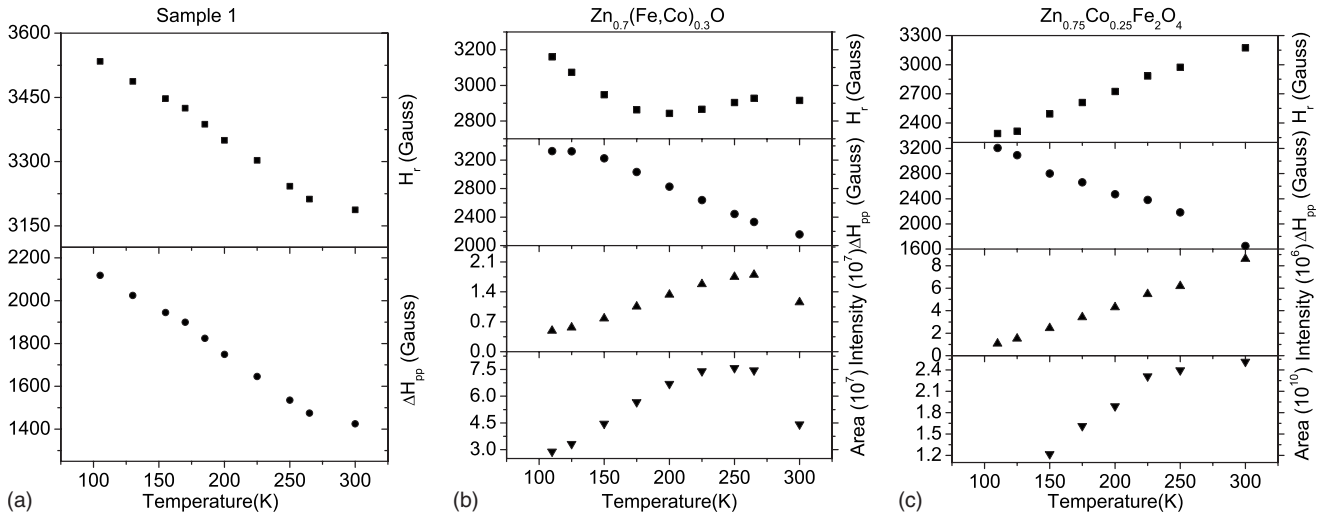

FIG. 18. Comparison of details of EPR signal for sample 1 is shown in the left panel of the figure. The temperature variation in line position (H_r) and linewidth (ΔH_{pp}) are plotted as a function of temperature. Comparison of details of EPR signal for sample 3 (middle panel) and $Zn_{0.75}Co_{0.25}Fe_2O_4$ (right panel) is shown in this figure. The temperature variation in line position (H_r), linewidth (ΔH_{pp}), intensity of the EPR line, and the area under the EPR line are plotted for sample 3 and doped ferrite sample. Due to complicated line shape, evaluation of intensity and area are not done for sample 1.

This indicates that the magnetic response of sample 3 contains the contribution from both ferrite phase as well as from the codoped ZnO. The intensity and area of the EPR lines, however, monotonically decrease with temperature as is also true for the ferrite sample. The increase in linewidth and decrease in area indicating the decrease in the percentage of coupled spins with lowering of temperature are also similar for sample 3 and ferrite phase.

In addition to this, for all these samples (1–3), Fe is always detected in the 3+ state. For the codoped system, presence of Fe^{3+} can be due to the following reasons. (a) Since the system is a nanocrystalline one, Fe^{2+} at the substitutional Zn site when resides on the surface of the nanoparticle, due to a gross variation in the nearest-neighbor coordination and presence of nearby cationic vacancies on the surface may lead to change in the valent state of surface TM ions from 2+ to 3+ (to neutralize the charge imbalance).[6] (b) Presence of segregated spinel phase in the system, where Fe^{3+} is present in the octahedral positions.

In the present case, for sample 1, as there is no segregated phase from XRD, presence of Fe^{3+} may be due to the former reason. For the other two samples, presence of higher valence state may be due to both of the reasons. It is also evident from the calculations of the formation energy for the codoped cluster that, the TM ions near the nanoparticle surface prefer to be in a higher valent configuration. However, in this paper, we could detect the valence states for Fe and Co as 3+ and 2+, respectively, due to the limitations of the experimental conditions.

For the ferrite system, presence of Fe^{3+} in the EPR spectra is expected from the spinel structure itself. However, due to the core-shell structure of the ferrite nanosystem, Fe may also be present in 2+ state in tetrahedral sites, where the core region is populated by spinel phase and the shell region closer to the surface consists of inverted spinel phase.[41,42] In the inverted-spinel phase, Fe ion is present both in octahedral (3+) and tetrahedral (2+) positions resulting in multiple valence in this material too.

Hence, from the detailed EPR measurement, we may conclude that although for a small doping percentage, the magnetic behavior seems to be predominantly for substitutional impurities, at higher percentage of doping, the magnetic behavior of the system has contributions from both codoped ZnO and segregated ferrite phases like Co-doped Zn ferrite.

IV. CONCLUSION

In conclusion, our first-principles electronic structure calculations suggest that for the (Fe,Co)-codoped bulk ZnO system, both with and without defects, irrespective of the system-size, tends to stabilize in a ferrimagnetic configuration, for a nearest-neighbor position of the TM dopants. The cluster calculations also indicate the ferrimagnetic state to be energetically most stable for the nearest-neighbor position of the codopants and the presence of unusual charge state of the codopants. However, the exact exchange behavior depends on the distance between the two TM ions and the position of the defects with respect to them, indicating a competitive mechanism of the parallel-spin double exchange versus antiparallel spin superexchange within the system. The experimental studies on the (Fe,Co)-codoped ZnO nanocrystal system, for lower dopant concentration, also reveal a similar competition between FI and FM behaviors within the sample as suggested by the theoretical results. Moreover, for higher dopant concentration, the presence of ferrite phases is indicated from the detailed investigation of the EPR spectra.

ACKNOWLEDGMENTS

G.P.D. and A.K.D. would like to thank BRNS for the support under CRP on Spintronics Materials. I.D. thanks DST, India for financial support.

[1] T. Dietl, H. Ohno, F. Matsukura, J. Cibert, and D. Ferrand, Science **287**, 1019 (2000).
[2] K. Ueda, H. Tabata, and T. Kawai, Appl. Phys. Lett. **79**, 988 (2001).
[3] Y. Fukuma, F. Odawara, H. Asada, and T. Koyanagi, Phys. Rev. B **78**, 104417 (2008).
[4] G. S. Chang, E. Z. Kurmaev, D. W. Boukhvalov, L. D. Finkelstein, S. Colis, T. M. Pedersen, A. Moewes, and A. Dinia, Phys. Rev. B **75**, 195215 (2007).
[5] D. Rubi, J. Fontcuberta, A. Calleja, L. Aragonès, X. G. Capdevila, and M. Segarra, Phys. Rev. B **75**, 155322 (2007).
[6] D. Karmakar, S. K. Mandal, R. M. Kadam, P. L. Paulose, A. K. Rajarajan, T. K. Nath, A. K. Das, I. Dasgupta, and G. P. Das, Phys. Rev. B **75**, 144404 (2007).
[7] C. D. Pemmaraju, R. Hanafin, T. Archer, H. B. Braun, and S. Sanvito, Phys. Rev. B **78**, 054428 (2008).
[8] M. Gacic, G. Jakob, C. Herbort, H. Adrian, T. Tietze, S. Bruck, and E. Goering, Phys. Rev. B **75**, 205206 (2007).
[9] C. Song, K. W. Geng, F. Zeng, X. B. Wang, Y. X. Shen, F. Pan, Y. N. Xie, T. Liu, H. T. Zhou, and Z. Fan, Phys. Rev. B **73**, 024405 (2006).
[10] N. Sanchez, S. Gallego, and M. C. Munoz, Phys. Rev. Lett. **101**, 067206 (2008).
[11] T. Chanier, I. Opahle, M. Sargolzaei, R. Hayn, and M. Lannoo, Phys. Rev. Lett. **100**, 026405 (2008).
[12] E.-C. Lee and K. J. Chang, Phys. Rev. B **70**, 115210 (2004).
[13] Z. Sun, W. Yan, G. Zhang, H. Oyanagi, Z. Wu, Q. Liu, W. Wu, T. Shi, Z. Pan, P. Xu, and S. Wei, Phys. Rev. B **77**, 245208 (2008).
[14] P. Gopal and N. A. Spaldin, Phys. Rev. B **74**, 094418 (2006).
[15] T. Chanier, M. Sargolzaei, I. Opahle, R. Hayn, and K. Koepernik, Phys. Rev. B **73**, 134418 (2006).
[16] S. Lany, J. Osorio-Guillén, and A. Zunger, Phys. Rev. B **75**, 241203(R) (2007).
[17] J. M. D. Coey, M. Venkatesan, and C. B. Fitzerald, Nat. Mater. **4**, 173 (2005).
[18] A. Kaminski and S. Das Sarma, Phys. Rev. Lett. **88**, 247202 (2002).
[19] L. Bergqvist, O. Eriksson, J. Kudrnovsky, V. Drchal, P. Korzhavyi, and I. Turek, Phys. Rev. Lett. **93**, 137202 (2004).
[20] A. J. Behan, A. Mokhtari, H. J. Blythe, D. Score, X.-H. Xu, J. R. Neal, A. M. Fox, and G. A. Gehring, Phys. Rev. Lett. **100**, 047206 (2008).
[21] J. Li, S.-H. Wei, S.-S. Li, and J.-B. Xia, Phys. Rev. B **74**, 081201(R) (2006).
[22] Y. He, P. Sharma, K. Biswas, E. Z. Liu, N. Ohtsu, A. Inoue, Y. Inada, M. Nomura, J. S. Tse, S. Yin, and J. Z. Jiang, Phys. Rev. B **78**, 155202 (2008).
[23] M. H. F. Sluiter, Y. Kawazoe, P. Sharma, A. Inoue, A. R. Raju, C. Rout, and U. V. Waghmare, Phys. Rev. Lett. **94**, 187204 (2005).
[24] X. C. Liu, E. W. Shi, Z. Z. Chen, H. W. Zhang, B. Xiao, and L. X. Song, Appl. Phys. Lett. **88**, 252503 (2006).
[25] D. Iusan, R. Knut, B. Sanyal, O. Karis, O. Eriksson, V. A. Coleman, G. Westin, J. M. Wikberg, and P. Svedlindh, Phys. Rev. B **78**, 085319 (2008).
[26] N. N. Lathiotakis, A. N. Andriotis, and M. Menon, Phys. Rev. B **78**, 193311 (2008).
[27] M. S. Park and B. I. Min, Phys. Rev. B **68**, 224436 (2003).
[28] Y. M. Cho, W. K. Choo, H. Kim, D. Kim, and Y. E. Ihm, Appl. Phys. Lett. **80**, 3358 (2002).
[29] O. K. Andersen, Phys. Rev. B **12**, 3060 (1975).
[30] V. V. Nemoshkalenko, A. E. Krasovskii, V. N. Antonov, Vl. N. Antonov, U. Fleck, H. Wonn, and P. Ziesche, Phys. Status Solidi B **120**, 283 (1983).
[31] M. T. Czyżyk and G. A. Sawatzky, Phys. Rev. B **49**, 14211 (1994).
[32] J. P. Perdew and Y. Wang, Phys. Rev. B **45**, 13244 (1992).
[33] J. P. Perdew, K. Burke, and M. Ernzerhof, Phys. Rev. Lett. **77**, 3865 (1996).
[34] V. I. Anisimov, F. Aryasetiawan, and A. I. Lichtenstien, J. Phys.: Condens. Matter **9**, 767 (1997).
[35] G. Kresse and J. Hafner, Phys. Rev. B **47**, 558 (1993).
[36] G. Kresse and J. Furthmüller, Phys. Rev. B **54**, 11169 (1996).
[37] P. E. Blöchl, Phys. Rev. B **50**, 17953 (1994).
[38] N. Ganguli, I. Dasgupta, and B. Sanyal, Appl. Phys. Lett. **94**, 192503 (2009).
[39] A. C. Reber, S. N. Khsnna, J. S. Hunjan, and M. R. Beltran, Chem. Phys. Lett. **428**, 376 (2006).
[40] A. F. Kohan, G. Ceder, D. Morgan, and Chris G. Van de Walle, Phys. Rev. B **61**, 15019 (2000).
[41] J. H. Shim, T. Hwang, S. Lee, J. H. Park, S.-J. Han, and Y. H. Jeong, Appl. Phys. Lett. **86**, 082503 (2005).
[42] J. H. Shim, S. Lee, J. H. Park, S. J. Han, Y. H. Jeong, and Y. W. Cho, Phys. Rev. B **73**, 064404 (2006).
[43] M. D. Sastry, K. S. Ajayakumar, R. M. Kadam, G. M. Pathak, and R. M. Iyer, Physica C **170**, 41 (1990).
[44] J. Hays, K. M. Reddy, N. Y. Graces, M. H. Engelhard, V. Shutthanandan, M. Luo, C. Xu, N. C. Giles, C. Wang, S. Thevuthasan, and A. Punnose, J. Phys.: Condens. Matter **19**, 266203 (2007).
[45] N. Jedrecy, H. J. von Bardeleben, Y. Zheng, and J.-L. Cantin, Phys. Rev. B **69**, 041308(R) (2004).
[46] T. Kataoka, M. Kobayashi, Y. Sakamoto, G. S. Song, A. Fujimori, F.-H. Chang, H.-J. Lin, D. J. Huang, C. T. Chen, T. Ohkochi, Y. Takeda, T. Okane, Y. Saitoh, H. Yamagami, A. Tanaka, S. K. Mandal, T. K. Nath, D. Karmakar, and I. Dasgupta, J. Appl. Phys. **107**, 033718 (2010).
[47] S. P. Gubin, Yu. I. Spichnin, Yu. A. Koksharov, G. Yu. Yorkov, A. V. Kozinkin, T. I. Nedoseikina, M. S. Korobov, and A. M. Tishin, J. Magn. Magn. Mater. **265**, 234 (2003).
[48] O. Santini, A. R. de Moraes, D. H. Mosca, P. E. N. de Souza, A. J. A. de Oliveira, R. Marangoni, and F. Weypych, J. Colloid Interface Sci. **289**, 63 (2005).
[49] V. G. Pol, M. Motiei, A. Gedanken, J. Calderon-Moreno, and Y. Mastei, Chem. Mater. **15**, 1378 (2003).